Facet-Dependent Gas Adsorption Selectivity on ZnO

Document Version:
Publisher's PDF, also known as Version of Record (includes final page, issue and volume numbers)

Please check the document version of this publication:

• A submitted manuscript is the version of the article upon submission and before peer-review. There can be important differences between the submitted version and the official published version of record. People interested in the research are advised to contact the author for the final version of the publication, or visit the DOI to the publisher's website.
• The final author version and the galley proof are versions of the publication after peer review.
• The final published version features the final layout of the paper including the volume, issue and page numbers.
Link to publication

Article

Facet-Dependent Gas Adsorption Selectivity on ZnO: A DFT Study

Weile Jiang [1,†]**, Yong Xia** [2,3,*,†]**, Aifei Pan** [3]**, Yunyun Luo** [2,3]**, Yaqiong Su** [4,5]**, Sikai Zhao** [6]**, Tao Wang** [2,3] **and Libo Zhao** [2,3]

[1] School of Humanities and Social Science, Institute of Heritage Sites & Historical Architecture Conservation, Xi'an Jiaotong University, Xi'an 710049, China

[2] State Key Laboratory for Manufacturing Systems Engineering, International Joint Laboratory for Micro/Nano Manufacturing and Measurement Technologies, Xi'an Jiaotong University (Yantai) Research Institute for Intelligent Sensing Technology and System, Xi'an Jiaotong University, Xi'an 710049, China

[3] School of Mechanical Engineering, Xi'an Jiaotong University, Xi'an 710049, China

[4] School of Chemistry, Xi'an Key Laboratory of Sustainable Energy Materials Chemistry, Xi'an Jiaotong University, Xi'an 710049, China

[5] Laboratory of Inorganic Materials & Catalysis, Schuit Institute of Catalysis, Eindhoven University of Technology, P.O. Box 513, 5600 MB Eindhoven, The Netherlands

[6] School of Resources and Civil Engineering, Northeastern University, Shenyang 110819, China

[*] Correspondence: xia395714753@stu.xjtu.edu.cn

[†] These authors contributed equally to this work.

Abstract: Semiconductor-based gas sensors are of great interest in both industrial and research settings, but poor selectivity has hindered their further development. Current efforts including doping, surface modifications and facet controlling have been proved effective. However, the "methods-selectivity" correlation is ambiguous because of uncontrollable defects and surface states during the experiments. Here, as a case study, using a DFT method, we studied the adsorption features of commonly tested gases—CH_2O, H_2, C_2H_5OH, CH_3COCH_3, and NH_3—on facets of $ZnO(000\bar{1})$, $ZnO(10\bar{1}0)$ and $ZnO(10\bar{1}1)$. The adsorption energies and charge transfers were calculated, and adsorption selectivity was analyzed. The results show $ZnO(000\bar{1})$ has obvious CH_2O adsorption selectivity; $ZnO(10\bar{1}0)$ has a slight selectivity to C_2H_5OH and NH_3; and $ZnO(10\bar{1}1)$ has a slight selectivity to H_2, which agrees with the experimental results. The mechanism of the selective adsorption features was studied in terms of polarity, geometric matching and electronic structure matching. The results show the adsorption selectivity is attributed to a joint effort of electronic structure matching and geometric matching: the former allows for specific gas/slab interactions, the latter decides the strength of the interactions. As the sensing mechanism is probably dominated by gas–lattice interactions, this work is envisioned to be helpful in designing new sensing material with high selectivity.

Keywords: semiconductor-based gas sensors; gas adsorption selectivity; ZnO facets; DFT calculations; electronic and geometric matching

1. Introduction

Due to high sensitivity, fast response, low cost and ease of fabrication and integrations, semiconductor-based gas sensors have been extensively used in leak alarms, pollution monitoring, building air quality control and heritage conservation airborne pollution monitors, etc. [1–3]. However, one of the biggest challenges of these sensors is poor selectivity, which hinders their further application [4,5]. To deal with this well-known challenge, researchers have developed a variety of methods, which can be divided into two types, i.e., indirect and direct. The indirect methods include using specific gas filters [6] and introducing the other output parameters apart from resistance, namely "multi-variable outputs", such as pulse heating-induced parameters [7] and impedance-related parameters [8,9]. The indirect

methods usually solve the challenge of selectivity perfectly at the initial stage. However, they might suffer from uncontrollable selectivity output along with the fading processes of the sensing materials and devices because complex parameters and algorithms make it hard to correct the selectivity. Worse still, the added complexity of the sensing system could greatly weaken the existing merits of the semiconductor-based gas sensors. The other type of method is the direct design of the sensing materials with high selectivity, which is much simpler and more efficient. The direct methods include heteroatom doping [10,11], facet controlling [12,13] and surface functioning [1,2,14], etc. Although great progress has been made in the past decade, the unambiguously correlated "methods-selectivity" relation is hard to achieve because of uncontrollable defect states, surface status and material stacking morphologies during the experiments [5,15], which severely hinders the development of new selective sensing materials.

Currently, some researchers have used density function theory (DFT) to analyze the semiconductor-based gas sensing properties and successfully explained the experimental results [1,16]. However, most calculations mainly focus on specific new materials in terms of doping or surface functioning; few contribute to the facet-dependent selectivity, even though it has been extensively studied by experiments due to ease of control and apparent structure selectivity correlations [15,17,18].

Here, by using the DFT method, we studied the most commonly seen ZnO facets of $(000\bar{1})$, $(10\bar{1}0)$ and $(10\bar{1}1)$ [13,15,19,20] and the adsorption features of the most commonly tested gases (CH_2O, H_2, C_2H_5OH, CH_3COCH_3, NH_3) [2,13,15,20–24] on these facets. The adsorption selectivity and possible mechanisms were systematically investigated and analyzed. The choice of ZnO is because of it is ease of being synthesized in the form of single crystals with specific facet exposure. The choice of the $(000\bar{1})$ facet of ZnO is because of its higher stability in air [25], which is representative in the air background sensing environment. Similarly, O-terminated ZnO $(10\bar{1}1)$ was studied instead of the Zn-terminated one. O_2 is not considered here, since this work mainly focuses on the "adsorption" process instead of the "adsorption and transduction" process of gas sensing [26]. Additionally, it has been pointed out that the sensing mechanism might be that the gases interact with lattice O on the surfaces, which causes a change of surface conductivity, and the O_2 in the air helps to restore the surface conductivity [27]. Out previous work also clearly showed this possibility, since the ethanol response in an N_2 background is much higher than in the air background [14].

2. Computation Methods

All calculations were performed using the Vienna ab initio simulation package (VASP) based on the DFT framework [28]. The projector-augmented wave (PAW) with cut-off energy of 450 eV was adopted to describe the ion–electron interaction [29]. The gradient approximation (GGA) with the Perdew–Burke–Ernzerhof (PBE) exchange correlation function was adopted to describe the electron exchange correlation [30]. During calculations, the Zn ($3d^{10}$, $4p^2$), O ($2s^2$, $2p^4$), H ($1s^1$) and C ($2s^2 2p^2$) were treated as valence electrons.

Slabs of $ZnO(000\bar{1})$, $ZnO(10\bar{1}0)$ and $ZnO(10\bar{1}1)$ surfaces with 96 atoms (Zn48O48) were built by cleaving the optimized wurtzite primary cell along corresponding directions, with a thickness of four bilayers and supercells of 3×2. A vacuum layer of 15 Å was added to the top along the z direction to get rid of interactions between periodic image structures. During surface calculations, the bottom two bilayers were fixed, and the two top bilayers were allowed to relax. For the Brillouin zone integration, gamma-centered k-point mesh densities of $3 \times 3 \times 1$ and $4 \times 4 \times 1$ were adopted for geometry optimization and electron structure calculation, respectively.

Gases of hydrogen (H_2), ammonia (NH_3), formaldehyde (CH_2O), ethanol (C_2H_5OH) and acetone (CH_3COCH_3) were pre-optimized from available conformations [31] using gamma point in a box of $20 \times 20.01 \times 20.02$ Å^3 before adsorption calculations. The convergence criterion for geometry optimization and electron structure calculation were set as 1×10^{-5} eV and 1×10^{-6} eV, respectively, with force convergence set to 0.01 eV/Å.

During calculations, the DFT-D3 correction proposed by Grimme [32] was adopted to correct the dispersion force.

The gas adsorption selectivity of various gases on specific surface slabs was evaluated via adsorption energy, which can be calculated as:

$$E_{\text{ads}} = E_{\text{slab-gas}} - E_{\text{gas}} \tag{1}$$

where $E_{\text{slab-gas}}$ and E_{gas} are the energies of gas adsorption systems and isolated gases, respectively.

To clarify the charge transfer during gas adsorption, Bader charge was calculated using the code developed by the Henkelman group [33]. Additionally, the charge differences during gas adsorption were visualized via calculating the charge density difference (CDD) and visualizing in VESTA [34], as explained in our last work [35].

3. Results

3.1. Surface Properties

To understand the differences among the interested ZnO facets, slabs of $\text{ZnO}(000\bar{1})$, $\text{ZnO}(10\bar{1}0)$ and $\text{ZnO}(10\bar{1}1)$ were built and relaxed. The relaxed slabs are shown in Figure 1. Figure 1a is the bulk wurtzite ZnO model projected along $[1\bar{2}10]$, which clearly illustrates $\{10\bar{1}1\}$, $\{0001\}$ and $\{10\bar{1}0\}$ facets.
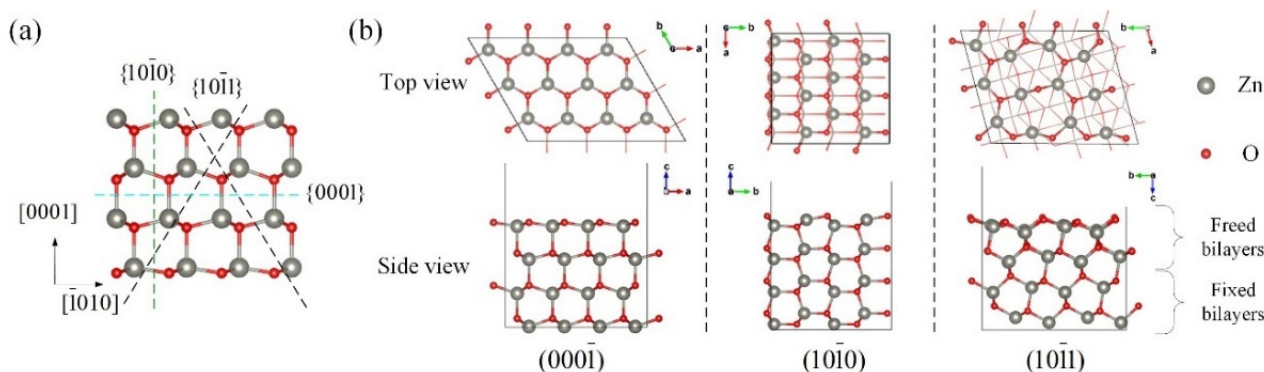

Figure 1. The studied facets, their positions and correspondingly relaxed slabs. (**a**) Atomic model of wurtzite ZnO projected along $[1\bar{2}10]$, showing $\{10\bar{1}1\}$, $\{0001\}$ and $\{10\bar{1}0\}$ facets. (**b**) The relaxed slabs of $\text{ZnO}(000\bar{1})$, $\text{ZnO}(10\bar{1}0)$ and $\text{ZnO}(10\bar{1}1)$, respectively. Vacuum layers were set along c axes. Explicitly, in the top view, all bilayers except the first bilayer are shown with a wireframe.

Figure 1b portrays relaxed slabs of $\text{ZnO}(000\bar{1})$, $\text{ZnO}(10\bar{1}0)$ and $\text{ZnO}(10\bar{1}1)$, respectively. For $\text{ZnO}(000\bar{1})$, the surface is terminated only by O ions, which results in polarity. The O ions in the first layer relaxed inward, which agrees well with previous results [36]. For $\text{ZnO}(10\bar{1}0)$, terrace structures with O and Zn ions alternatively arranged on the surface. In the uppermost surface layers (the "freed bilayers"), the O ions remain almost in bulk positions with small relaxations away from the surface; the Zn ions relax inward (0.33 Å) and a movement (0.20 Å) parallel to the surface (b axis), which agree well with the measured values of 0.40 Å [37] and theoretical studies of 0.16 Å [38], respectively. For $\text{ZnO}(10\bar{1}1)$, the surface is terminated by O ions only. Thus, the polarity is expected. The upmost O ions relax strongly due to fewer coordination features.

The calculated surface properties can be calculated as:

$$E_{\text{surf}} = \frac{1}{2A}(E_{\text{slab}} - N \times E_{\text{bulk}}) \tag{2}$$

where A, E_{slab}, N, E_{bulk} are the surface area, total energy of a surface slab, number of Zn-O units in the slab, energy per Zn-O unit in the bulk material, respectively.

The calculated surface energies along with system energies and coordination numbers of Zn/O ions in the first bilayer are tabulated in Table 1. Due to the asymmetric feature when cutting a solid into two polar surfaces, the surface energies of an O-terminated polar surface might be overestimated, as the Zn-terminated surfaces usually have higher surface energies [39]. Nevertheless, the obtained trend agrees with the published results [25,39–41], i.e., the fewer coordinated ions the surface has, the higher the surface energy. In addition, it has been found that the surface energy is correlated to the surface catalytic activity [42]. Therefore, the gas-slab interaction of $ZnO(10\bar{1}1)$ is foreseen to be the strongest.

Table 1. Surface properties of $ZnO(000\bar{1})$, $ZnO(10\bar{1}0)$ and $ZnO(10\bar{1}1)$ after relaxation.

Surface	Atoms	System Energy (eV)	Coordination Number of O on the 1st Bilayer	Coordination Number of Zn on the 1st Bilayer	Surface Energy (J/m²)	
					This Work	Ref.
$ZnO(000\bar{1})$	Zn48O48	−406.12	3	4	1.39	1.01 [39]; 0.96 [25]
$ZnO(10\bar{1}0)$	Zn48O48	−415.41	4, 3	4, 3	0.87	0.91 [40]; 0.82 [39]; 1.12 [41]
$ZnO(10\bar{1}1)$	Zn48O48	−395.93	3, 2	4	2.00	1.74 [40]

3.2. Adsorption Configuration

The calculated adsorption conformations with the lowest energy are shown in Figure 2. For $ZnO(000\bar{1})$, CH_2O adsorbs vertically and decomposes H atoms; H_2 and CH_3COCH_3 adsorb horizontally over the surface, which indicates weak interactions with the slab; C_2H_5OH adsorbs vertically with a distance of 1.635 Å via interactions between its hydroxyl group with lattice O (O_L); NH_3 absorbs on lattice Zn via its N atom and all H atoms are aligned to specific O_L ions. For $ZnO(10\bar{1}0)$, due to terrace structures alternatively arranged with Zn and O ions, all adsorbents adsorb on the slab in a structure of bridging the O_L and lattice Zn, except the case of H_2. For $ZnO(10\bar{1}1)$, all gases adsorb and dehydrogenate on the less coordinated O_L, except CH_3COCH_3. Nevertheless, there is a strong surface reconstruction during CH_3COCH_3 adsorption. In addition, it is noticed that when NH_3 adsorb, a destructive adsorption of forming aminoxide happens.
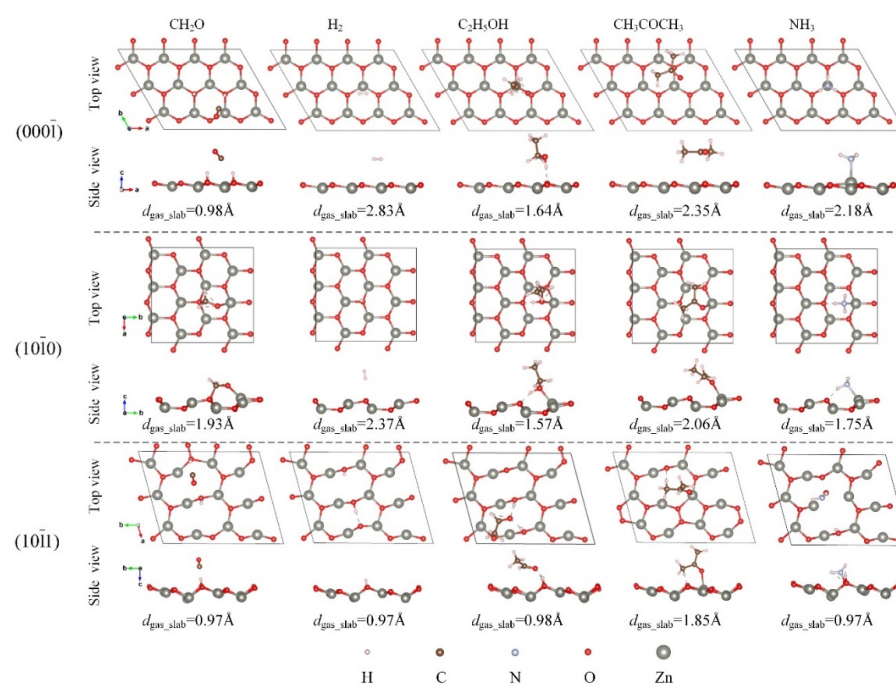

Figure 2. The optimized gas adsorption conformations on $ZnO(000\bar{1})$, $ZnO(10\bar{1}0)$ and $ZnO(10\bar{1}1)$. To clearly illustrated the gas–slab interactions, only the first bilayer of slabs is shown.

3.3. Adsorption Energy and Charge Transfer

To understand the interactions between gases and slabs, the adsorption energy and Bader charge were calculated, and the results are shown in Figure 3 and Table S1. For $ZnO(000\bar{1})$, apart from the decomposed CH_2O, which has a high adsorption energy of -4.13 eV, the other four gases show much less adsorption energy, and in an order of NH_3 (-0.66 eV) > C_2H_5OH (-0.64 eV) > CH_3COCH_3 (-0.34 eV) > H_2 (-0.11 eV). A similar trend is also found in charge transfer. Therefore, the results show $ZnO(000\bar{1})$ has adsorption selectivity to CH_2O.
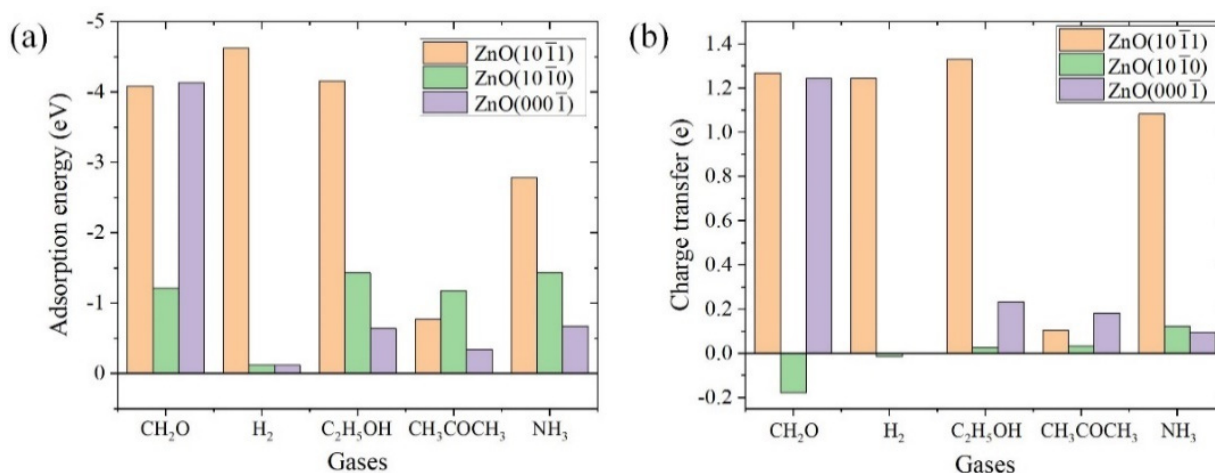

Figure 3. Adsorption energies (**a**) and charge transfers (**b**) of the adsorption systems.

For $ZnO(10\bar{1}0)$, adsorption energies of CH_2O, H_2, C_2H_5OH, CH_3COCH_3 and NH_3 are -1.21, -0.12 -1.43, -1.17 and -1.44 eV, respectively. Only a slight selectivity to C_2H_5OH and NH_3 is observed. Interestingly, the charge transfer results show negative values when CH_2O and H_2 adsorb on $ZnO(10\bar{1}0)$, and a relatively small value in the case of C_2H_5OH.

For $ZnO(10\bar{1}1)$, adsorption energies of CH_2O, H_2, C_2H_5OH, CH_3COCH_3 and NH_3 are -4.08, -4.62, -4.16 eV, -0.77 and -2.78 eV, respectively. The gas adsorption energies are much higher than on the other slabs due to dehydrogenation. A slight selectivity to H_2 of the slab is shown. The charge transfer shows a similar trend as the adsorption energy, but H_2 shows a relatively lower charge transfer.

Additionally, to understand how charge transfer happens during gas adsorption, CDD of the systems were calculated, and the results are shown in Figure 4.

For $ZnO(000\bar{1})$, it is noticed that the decomposed H atoms of CH_2O show strong interactions with O_L, as intense isosurfaces of charge overlap, while the remaining C-O has no obvious contribution. H_2 interacts weakly with both O_L and Zn, of which the saturated isosurface value is set as 4% of the default value (0.05 e/bohr^3). It accepts electrons from Zn ions and donates electrons to O_L ions simultaneously, which further lowers the charge transfer to a negligible value. C_2H_5OH donates electrons via H–O_L interactions of the hydroxyl group. CH_3COCH_3 donates electrons via H atoms of the methyl group and C atoms of the ketone group. NH_3 donates electrons via H–O_L interactions, and accepts electrons via N–Zn interactions, resulting in little charge transfer.

For $ZnO(10\bar{1}0)$, CH_2O donates and accepts electrons via C–O_L and O–Zn interactions, respectively. Due to stronger electronegativity differences of O–Zn compared with C–O_L, the net charge transfer is negative. Similarly, C_2H_5OH, CH_3COCH_3 and NH_3 adsorb with a bridge structure that donates and accepts electrons simultaneously. The difference is that those molecules donate electrons via H–O_L interactions, and therefore, the charge transfers are positive. The small values of the charge transfer can be attributed to weak interactions due to large H–O_L distances. The relatively higher charge transfer value of NH_3 can be explained by weaker electronegativity of N in NH_3 compared with O, which limits its ability in obtaining electrons from the Zn ions on the slab. The absorption conformation

of H_2 is far away from the slab (2.37 Å), and the H atom weakly interacts with O_L, which results in little charge transfer.
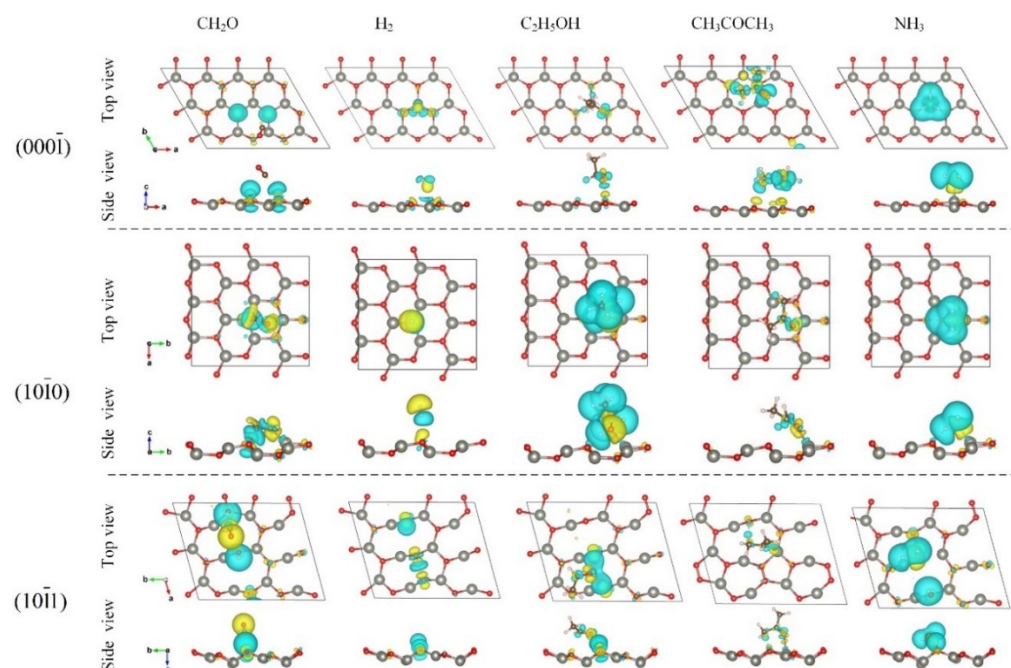

Figure 4. The charge density difference (CDD) of the adsorption systems. The blue and yellow isosurfaces are charge depletion and accumulation areas, respectively. The isosurface values are set to 0.0002 e/bohr^3 for H_2/ZnO$(000\bar{1})$ and H_2/ZnO$(10\bar{1}0)$, 0.001 e/bohr^3 for CH_3COCH_3/ZnO$(000\bar{1})$ and 0.005 e/bohr^3 for the other systems as the default value, respectively. For clarity, only the first bilayer is shown.

For ZnO$(10\bar{1}1)$, due to adsorption conformations with H decomposition, CH_2O, H_2, C_2H_5OH and NH_3 donate lots of electrons via dehydrogenation. CH_3COCH_3 donates electrons via H–O_L interactions and accepts electrons via O–Zn interactions. Therefore, a comparable charge transfer is obtained as on the slab of ZnO$(10\bar{1}0)$, even though ZnO$(10\bar{1}1)$ is more reactive due to less coordinated O_L.

4. Selectivity Analysis and Mechanism Discussion

As discussed above, ZnO$(000\bar{1})$ shows good selectivity for CH_2O adsorption; ZnO$(10\bar{1}0)$ has a slight selectivity to C_2H_5OH and NH_3, and all gases except H_2 show comparable adsorption energies. ZnO$(10\bar{1}1)$ has a slight selectivity to H_2, and all gases except CH_3COCH_3 can adsorb and decompose on the surface. For comparison, the gas adsorption selectivity is listed along with the published experimental results in gas sensing, as shown in Table 2. It is shown that the calculated adsorption selectivity roughly agrees with the experimental results, i.e., ZnO$(000\bar{1})$ has adsorption selectivity to CH_2O and C_2H_5OH; ZnO$(10\bar{1}0)$ has adsorption selectivity to NH_3 and C_2H_5OH; ZnO$(10\bar{1}1)$ has adsorption selectivity to H_2, C_2H_5OH and CH_2O, and $H_2 > C_2H_5OH$, CH_2O. The unmatched part can be attributed to: (1) there might be various surface states, such as defects and contaminations or coatings, that are not considered in the calculations; (2) the differences between "adsorption selectivity" and "sensing selectivity", where the latter possesses the other process of "transduction" apart from "adsorption".

Table 2. Comparison between the calculated selectivity and the published experimental results.

ZnO Facets	Calculated Adsorption Selectivity	Gas Sensing Selectivity by Experiments
$ZnO(000\bar{1})$	CH_2O [1] $> NH_3, C_2H_5OH > CH_3COCH_3 > H_2$	C_2H_5OH (s) [2] [13,15,20], C_2H_5OH, CH_2O (s) [21]
$ZnO(10\bar{1}1)$	$NH_3, C_2H_5OH > CH_2O > CH_3COCH_3 > H_2$	CH_2O (p) [2]; C_2H_5OH (s) [13,15,20]; C_2H_5OH, CH_3COCH_3 (s) [22]; C_2H_5OH, CH_2O (s) [21]; NH_3 (s) [10]
$ZnO(10\bar{1}1)$	$H_2 > C_2H_5OH > CH_2O > NH_3 > CH_3COCH_3$	CH_2O (p) [2]; C_2H_5OH (s) [13,24]; NH_3 (s) [10]; H_2 (p) [23]

[1] The selectivity to CH_2O is obvious. [2] The "s" in the bracket denotes the material is a ZnO single crystal; "p" in the bracket denotes ZnO polycrystal nanoparticles or grains.

To further understand the mechanism of the adsorption selectivity, polarity, electrostatic potential and electronic structure of both gases and slabs were further studied.

4.1. Polarity

It is reported that polarity plays an important role in gas sensing selectivity, such as selectivity to CH_3COCH_3 over C_2H_5OH [4]. Here, the experimental polarities of the gases are listed in Table 3. The polarity of gases can be listed in an order of $CH_3COCH_3 > CH_2O > C_2H_5OH > NH_3$, while H_2 is nonpolar. When compared to gas adsorption results shown in Figure 3a, it can be found that polarity seems to be true in the case of $H_2/ZnO(000\bar{1})$, where other polar gases show higher adsorption energies. However, it might be hard to explain the highest adsorption energy of H_2 on the polar surface of $ZnO(10\bar{1}1)$. In addition, the order of adsorption energies on the typical polar surface of $ZnO(000\bar{1})$ does not match with the polarity of the gases. Therefore, our calculated results do not show evidence of polarity influences on selectivity.

Table 3. Experimental polarity of the studied gases [43].

Gases	CH_3COCH_3	CH_2O	C_2H_5OH	NH_3	H_2
Dipole moment (Debye)	2.88	2.33	1.52	1.48	0

4.2. Geometric Matching and Electrostatic Interactions

The electrostatic potential is another important factor that has been considered for interface adsorption [44,45]. The electrostatic potential mapping onto electron isosurfaces of the gas molecules according to ref. [45] are shown in Figure 5. The CH_2O has a symmetrical electrostatic potential along its vertical conformation, where the O atom is in negative potential and C/H atoms are in positive potential, as shown in Figure 5a. Figure 5b shows an unsymmetrical potential around C_2H_5OH, where the potential near the O atom is -171.17 kJ/mol, and potentials near the other atoms are positive, with the highest value of 230.96 kJ/mol showing up near the H atom of the hydroxyl group. Figure 5c shows an unsymmetrical electrostatic potential around the CH_3COCH_3 molecule, with a bigger negative potential near the O atom and positive potential near the other atoms. Figure 5d shows an unsymmetrical electrostatic potential around NH_3, where the bigger negative potential of -226.60 kJ/mol is near N and the smaller positive value of 145.71 kJ/mol near the other three H atoms. Figure 5f shows the electrostatic potential around H_2, where the positive potential is around two ends and the negative potential in the middle.
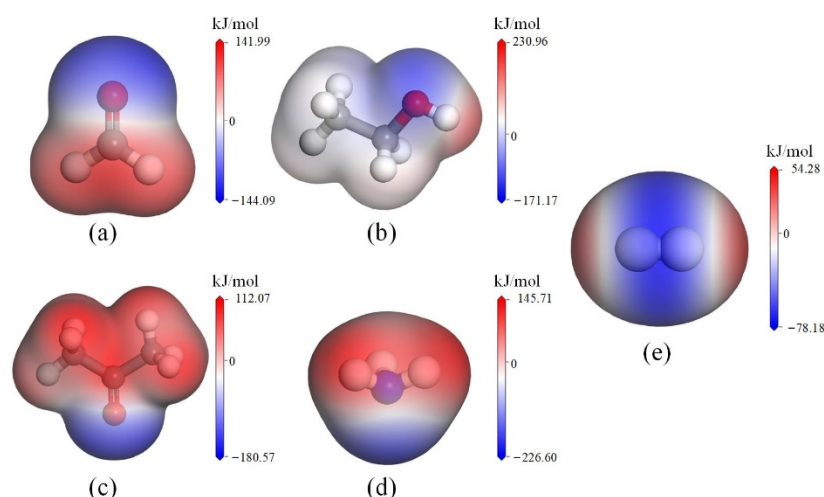
Figure 5. Molecular structures and computed electrostatic potentials on electron isosurfaces of (**a**) CH_2O, (**b**) C_2H_5OH, (**c**) CH_3COCH_3, (**d**) NH_3 and (**e**) H_2.

Due to the larger electronegativity of O compared with Zn [46], O ions accumulate electrons, while Zn ions deplete electrons, resulting in the negative potential of O and the positive potential of Zn. The calculated Bader charge states of O/Zn ions in specific slabs are shown in Figure S1 and Table S2. Combining with the adsorption conformations in Figure 2, it is found the gases prefer to adsorb on the slab with the atom that has the biggest electrostatic potential, and the adsorption sites are usually the opposite charge to the atom.

As a result, CH_2O prefers to adsorb on the ZnO slabs with $H/C–O_L$ and $O–Zn$ interactions, respectively. C_2H_5OH prefers to adsorb with $H–O_L$ interactions in the hydroxyl group. CH_3COCH_3 prefers to adsorb with $O–Zn$ interactions. NH_3 prefers to adsorb with $N–Zn$ interactions or $N–O_L$ interactions due to long pairs. H_2 prefers to adsorb with one side towards O_L or the central part close to Zn. Due to the surfaces of $ZnO(000\bar{1})$ and $ZnO(10\bar{1}1)$ being terminated with O, CH_2O adorbs on the surfaces with two H atoms. Since lattice parameters of the slab surface match the molecule binding sites, the adsorbed CH_2O decomposed into adsorbed H atoms and isolated CO, as schematically shown in Figure 6. Since the preferred adsorption sites of the other gases cannot match the surface lattice of $ZnO(000\bar{1})$, only CH_2O exhibits obviously selective adsorption.
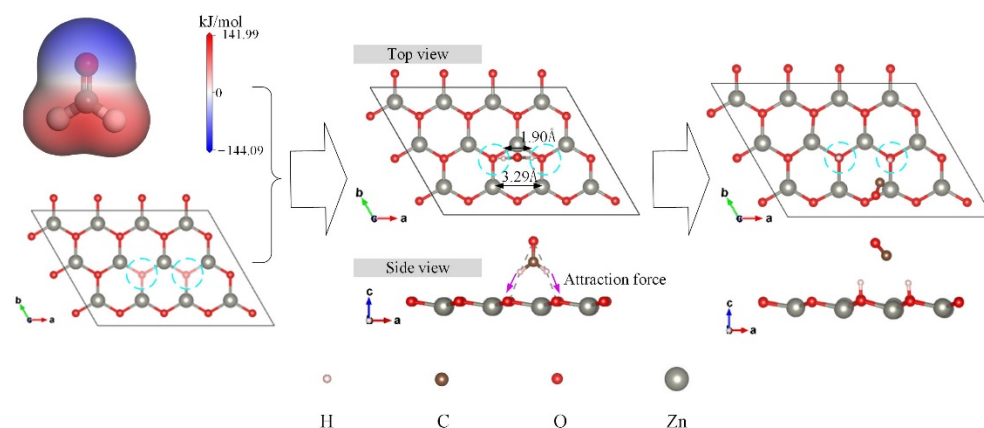

Figure 6. Schematic view of CH_2O adsorption and decomposition on the surface of $ZnO(000\bar{1})$.

As for $ZnO(10\bar{1}1)$, due to high chemical activity of the less coordinated O_L ions (as shown in Figure S1 and Table S2), the H bond in the gas molecules is vulnerable. As a result, H_2, CH_2O, C_2H_5OH and NH_3 all show high adsorption energies during adsorption on the surface. The geometric matching between the adsorption sites and the surface lattice allows for a slightly higher adsorption selectivity for H_2. As for $ZnO(10\bar{1}0)$, it is

because of its Zn/O_L alternative terrace structure that CH_2O, C_2H_5OH, CH_3COCH_3 and NH_3 can adsorb with a "bridge" conformation. In addition, all these molecules show high adsorption energies.

Therefore, geometry matching between the surface lattice and the adsorption sites indeed plays an important role in gas adsorption selectivity based on our calculations.

4.3. Electronic Structure Matching

In addition to geometry matching, the electronic structures of the slabs and the gases were also considered. The calculated highest occupied molecular orbital (HOMO) and lowest unoccupied molecular orbital (LUMO) energies of the gases are tabulated in Table S4, which agrees well with the data in the Benchmark DataBase of NIST [43]. The density of states (DOS) of the adsorption systems (gas molecule and slabs) before adsorption interactions are shown in Figure 7. The DOSs of gas molecules are the DOSs of isolated gases shifting to energy alignment with the specific slabs, and the DOSs of slabs are the projected DOSs of isolated slabs at O 2p/Zn 3d orbitals of the first bilayer. Additionally, since the Fermi energies calculated by VASP is set as the valence band maximum [47], here the Fermi energies of specific slabs were shifted according to their experimental work function [48–50], as illustrated in part 3 of the Supplementary Materials.

It is found that the HOMO energies of four gases (CH_2O, C_2H_5OH, CH_3COCH_3 and NH_3) are higher than the Fermi energies (E_f) of $ZnO(10\bar{1}0)$ and $ZnO(10\bar{1}1)$, but lower than the E_f of $ZnO(000\bar{1})$. The HOMO energy of H_2 is lower than the E_f of all slabs. All LUMO energies of the five gases are far higher than the E_f. Therefore, the possible gas–slab interactions are the interactions between the HOMO states of gas molecules and Zn/O states of the slabs in the valence band. It is beneficial when HOMO energy is higher than E_f, since the energies of antibonding states would be higher than E_f during gas–slab interactions. The higher energy of antibonding states dump electrons at the Fermi level, which keeps the adsorption system stable [51].

Therefore, for $ZnO(000\bar{1})$, no gas is expected to interact with the slab strongly. Still, because the HOMO level of CH_2O, C_2H_5OH, NH_3 and CH_3COCH_3 is close to O 2p states and E_f at the same time, it has the possibility to interact with O 2p of the slab and form antibonding states that are higher than E_f. Due to the closer energy levels and the stronger interactions, weak adsorptions of these gases with smaller adsorption energy of CH_3COCH_3 are expected, which agrees with the calculated adsorption energies, except for the adsorbed and decomposed CH_2O.

For $ZnO(10\bar{1}0)$, due to HOMO of CH_2O, C_2H_5OH, NH_3 and CH_3COCH_3 being higher than the E_f of the slab, these four gases can form stable bonds with the slab and are expected to have high adsorption energies. The bigger energy difference between Zn 3d/O 2p and HOMO energy of CH_3COCH_3 limits the adsorption energy. Therefore, strong adsorptions of these gases with smaller adsorption energy of CH_3COCH_3 are expected, which agrees with the calculated adsorption energies, expect for minor differences among CH_2O, C_2H_5OH and NH_3.

Similarly, for $ZnO(10\bar{1}1)$, strong adsorptions of CH_2O, C_2H_5OH and NH_3 with smaller adsorption energy of CH_3COCH_3 are expected. The interaction strength should be $CH_2O >$ $C_2H_5OH > NH_3$, which is slightly different from the adsorption energy of $C_2H_5OH > CH_2O$ $> NH_3$, and it can be attributed to geometric matching-induced molecule decomposition and conformation relaxation. It is also noted that the calculated results show the H_2 can adsorb and decompose on $ZnO(10\bar{1}1)$ and has the highest adsorption energy among all gases. This indicates the HOMO states of H_2 might be able to interact with the O 2p states of the slab and form antibonding states over E_f.

Therefore, the matching analysis of the electronic structure between gases and slabs before interaction is helpful in understanding the adsorption preference, and the geometric matching-induced electrostatic interactions decide the molecule decomposition and conformation relaxation, which finally decides the gas adsorption selectivity.
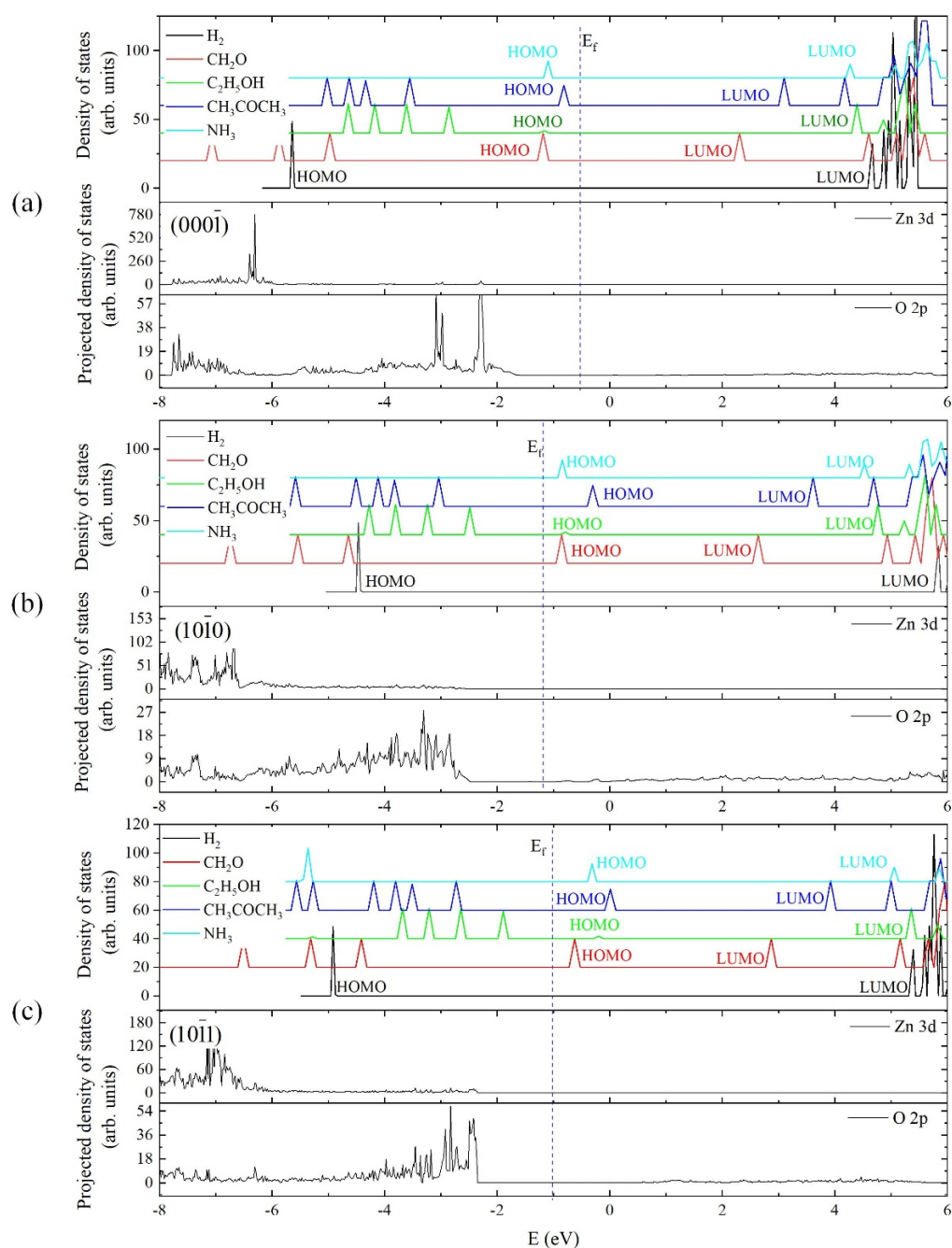
Figure 7. Density of states and projected density of states analysis for the adsorption systems of (**a**) ZnO$(000\bar{1})$, (**b**) ZnO$(10\bar{1}0)$ and (**c**) ZnO$(10\bar{1}1)$ before gas–slab interactions.

5. Conclusions

This work studied gas adsorption selectivity on three typical ZnO facets of ZnO$(000\bar{1})$, ZnO$(10\bar{1}0)$ and ZnO$(10\bar{1}1)$ using the DFT method. The adsorption conformations, adsorption energies and charge transfer features of the gases (CH$_2$O, H$_2$, C$_2$H$_5$OH, CH$_3$COCH$_3$ and NH$_3$) during adsorption were calculated and systematically analyzed. Based on these, the adsorption selectivity was evaluated and the mechanism beneath was analyzed in terms of polarity, geometric matching and electronic structure matching. It was found that: (1) the ZnO$(000\bar{1})$ has adsorption selectivity to CH$_2$O; (2) the ZnO$(10\bar{1}0)$ has high adsorption energies for C$_2$H$_5$OH, NH$_3$, CH$_2$O and CH$_3$COCH$_3$, with a slight selectivity to C$_2$H$_5$OH and NH$_3$; (3) the ZnO$(10\bar{1}1)$ has much better adsorption energies for CH$_2$O, C$_2$H$_5$OH, H$_2$ and NH$_3$, with a slight selectivity to H$_2$. We conclude the selectivity is attributed to

the geometric matching of the adsorption sites and surface lattices caused by electrostatic interactions and the electronic structure matching, which allows for the interactions.

However, since the work principle of semiconductor-based gas sensing is "adsorption-transduction", to better understand the experimental results and guide experimental works, future work will focus on "transduction" and the combination of "adsorption" and "transduction".

Supplementary Materials: The following supporting information can be downloaded at: https://www.mdpi.com/article/10.3390/chemosensors10100436/s1, Table S1: Calculated minimum distance; Figure S1: Schematic top view of the O/Zn ions in the slabs; Table S2: The Bader charge states of O/Zn ions; Figure S2: Schematic top view of atoms in $1 \times 2 \times 1$ supercell of $ZnO(000\bar{1})$ slab; Table S3: The Bader charge states of O/Zn ions in $ZnO(000\bar{1})$ supercell slab of $1 \times 2 \times 1$.

References

1. Liu, B.; Li, K.; Luo, Y.; Gao, L.; Duan, G. Sulfur spillover driven by charge transfer between AuPd alloys and SnO_2 allows high selectivity for dimethyl disulfide gas sensing. *Chem. Eng. J.* **2021**, *420*, 129881. [CrossRef]
2. Liu, J.; Zhang, L.; Cheng, B.; Fan, J.; Yu, J. A high-response formaldehyde sensor based on fibrous Ag-ZnO/In_2O_3 with multi-level heterojunctions. *J. Hazard. Mater.* **2021**, *413*, 125352. [CrossRef]
3. Shokrzadeh, L.; Mohammadi, P.; Mahmoudian, M.R.; Basirun, W.J.; Bahreini, M. L-glycine-assisted synthesis of SnO_2/Pd nanoparticles and their application in detection of biodeteriorating fungi. *Mater. Chem. Phys.* **2020**, *240*, 122172. [CrossRef]
4. Zhou, X.; Zou, Y.; Ma, J.; Cheng, X.; Li, Y.; Deng, Y.; Zhao, D. Cementing mesoporous ZnO with silica for controllable and switchable gas sensing selectivity. *Chem. Mater.* **2019**, *31*, 8112–8120. [CrossRef]
5. Kim, T.-H.; Jeong, S.-Y.; Moon, Y.K.; Lee, J.-H. Dual-mode gas sensor for ultrasensitive and highly selective detection of xylene and toluene using Nb-doped NiO hollow spheres. *Sens. Actuators B Chem.* **2019**, *301*, 127140. [CrossRef]
6. Broek, J.; Abegg, S.; Pratsinis, S.; Güntner, A. Highly selective detection of methanol over ethanol by a handheld gas sensor. *Nat. Commun.* **2019**, *10*, 4220. [CrossRef] [PubMed]
7. Suematsu, K.; Oyama, T.; Mizukami, W.; Hiroyama, Y.; Watanabe, K.; Shimanoe, K. Selective detection of toluene using pulse-driven SnO_2 micro gas sensors. *ACS Appl. Electron. Mater.* **2020**, *2*, 2913–2920. [CrossRef]
8. Potyrailo, R.A. Multivariable sensors for ubiquitous monitoring of gases in the era of internet of things and industrial internet. *Chem. Rev.* **2016**, *116*, 11877–11923. [CrossRef] [PubMed]
9. Liu, Y.; Lei, Y. Pt-CeO_2 nanofibers based high-frequency impedancemetric gas sensor for selective CO and C_3H_8 detection in high-temperature harsh environment. *Sens. Actuators B Chem.* **2013**, *188*, 1141–1147. [CrossRef]
10. Ganesh, R.S.; Durgadevi, E.; Navaneethan, M.; Patil, V.; Ponnusamy, S.; Muthamizhchelvan, C.; Kawasaki, S.; Patil, P.; Hayakawa, Y. Tuning the selectivity of NH_3 gas sensing response using Cu-doped ZnO nanostructures. *Sens. Actuators A Phys.* **2018**, *269*, 331–341. [CrossRef]
11. Song, L.; Dou, K.; Wang, R.; Leng, P.; Luo, L.; Xi, Y.; Kaun, C.-C.; Han, N.; Wang, F.; Chen, Y. Sr-doped cubic In_2O_3/rhombohedral In_2O_3 homojunction nanowires for highly sensitive and selective breath ethanol sensing: Experiment and DFT simulation studies. *ACS Appl. Mater. Interfaces* **2019**, *12*, 1270–1279. [CrossRef] [PubMed]
12. Jia, Q.-Q.; Ji, H.-M.; Wang, D.-H.; Bai, X.; Sun, X.-H.; Jin, Z.-G. Exposed facets induced enhanced acetone selective sensing property of nanostructured tungsten oxide. *J. Mater. Chem. A* **2014**, *2*, 13602–13611. [CrossRef]
13. Qin, N.; Xiang, Q.; Zhao, H.; Zhang, J.; Xu, J. Evolution of ZnO microstructures from hexagonal disk to prismoid, prism and pyramid and their crystal facet-dependent gas sensing properties. *CrystEngComm* **2014**, *16*, 7062–7073. [CrossRef]

14. Zhao, S.; Shen, Y.; Xia, Y.; Pan, A.; Li, Z.; Carraro, C. Maboudian, Synthesis and gas sensing properties of NiO/ZnO heterostructured nanowires. *J. Alloys Compd.* **2021**, *877*, 160189. [CrossRef]

15. Xu, J.; Xue, Z.; Qin, N.; Cheng, Z.; Xiang, Q. The crystal facet-dependent gas sensing properties of ZnO nanosheets: Experimental and computational study. *Sens. Actuators B Chem.* **2017**, *242*, 148–157. [CrossRef]

16. Zhou, T.; Chen, S.; Wang, X.; Xie, C.; Zeng, D. Catalytic activation of cobalt doping sites in ZIF-71-coated ZnO nanorod arrays for enhancing gas-sensing performance to acetone. *ACS Appl. Mater. Interfaces* **2020**, *12*, 48948–48956. [CrossRef]

17. Nikolic, M.V.; Milovanovic, V.; Vasiljevic, Z.Z.; Stamenkovic, Z. Semiconductor gas sensors: Materials, technology, design, and application. *Sensors* **2020**, *20*, 6694. [CrossRef]

18. Chen, Y.; Liu, B.; Liu, J.; Pei, C.; Zhao, H.; Shang, Y.; Yang, H. Enhancing gas-sensing property and sensing mechanism at molecule level of the hollow microspheres assembled with ZnO nanoflakes exposing {001} facets. *J. Mater. Sci. Mater. Electron.* **2020**, *31*, 6118–6129. [CrossRef]

19. Han, X.-G.; He, H.-Z.; Kuang, Q.; Zhou, X.; Zhang, X.-H.; Xu, T.; Xie, Z.-X.; Zheng, L.-S. Controlling morphologies and tuning the related properties of nano/microstructured ZnO crystallites. *J. Phys. Chem. C* **2009**, *113*, 584–589. [CrossRef]

20. Ju, D.; Xu, H.; Zhang, J.; Guo, J.; Cao, B. Direct hydrothermal growth of ZnO nanosheets on electrode for ethanol sensing. *Sens. Actuators B Chem.* **2014**, *201*, 444–451. [CrossRef]

21. Tian, H.; Fan, H.; Li, M.; Ma, L. Zeolitic imidazolate framework coated ZnO nanorods as molecular sieving to improve selectivity of formaldehyde gas sensor. *ACS Sens.* **2016**, *1*, 243–250. [CrossRef]

22. Zhou, T.; Sang, Y.; Wang, X.; Wu, C.; Zeng, D.; Xie, C. Pore size dependent gas-sensing selectivity based on ZnO@ ZIF nanorod arrays. *Sens. Actuators B Chem.* **2018**, *258*, 1099–1106. [CrossRef]

23. Kim, J.-H.; Mirzaei, A.; Kim, H.W.; Wu, P.; Kim, S.S. Design of supersensitive and selective ZnO-nanofiber-based sensors for H_2 gas sensing by electron-beam irradiation. *Sens. Actuators B Chem.* **2019**, *293*, 210–223. [CrossRef]

24. Jin, W.; Ma, S.; Tie, Z.; Xu, X.; Jiang, X.; Li, W.; Wang, T.; Lu, Y.; Yan, S. Synthesis of monodisperse ZnO hollow six-sided pyramids and their high gas-sensing properties. *Mater. Lett.* **2015**, *159*, 102–105. [CrossRef]

25. Tang, C.; Spencer, M.J.; Barnard, A.S. Activity of ZnO polar surfaces: An insight from surface energies. *Phys. Chem. Chem. Phys.* **2014**, *16*, 22139–22144. [CrossRef] [PubMed]

26. Degler, D.; Weimar, U.; Barsan, N. Current understanding of the fundamental mechanisms of doped and loaded semiconducting metal-oxide-based gas sensing materials. *ACS Sens.* **2019**, *4*, 2228–2249. [CrossRef]

27. Blackman, C. Do We Need "Ionosorbed" Oxygen Species? (Or, "A Surface Conductivity Model of Gas Sensitivity in Metal Oxides Based on Variable Surface Oxygen Vacancy Concentration"). *ACS Sens.* **2021**, *6*, 3509–3516. [CrossRef]

28. Hafner, J. Ab-initio simulations of materials using VASP: Density-functional theory and beyond. *J. Comput. Chem.* **2008**, *29*, 2044–2078. [CrossRef]

29. Kresse, G.; Furthmüller, J. Efficient iterative schemes for ab initio total-energy calculations using a plane-wave basis set. *Phys. Rev. B* **1996**, *54*, 11169. [CrossRef]

30. Perdew, J.P.; Burke, K.; Ernzerhof, M. Generalized gradient approximation made simple. *Phys. Rev. Lett.* **1996**, *77*, 3865. [CrossRef]

31. ChemSpider Search and Share Chemistry. Available online: http://www.chemspider.com/ (accessed on 14 October 2022).

32. Grimme, S.; Antony, J.; Ehrlich, S.; Krieg, H. A consistent and accurate ab initio parametrization of density functional dispersion correction (DFT-D) for the 94 elements H-Pu. *J. Chem. Phys.* **2010**, *132*, 154104. [CrossRef] [PubMed]

33. Tang, W.; Sanville, E.; Henkelman, G. A grid-based Bader analysis algorithm without lattice bias. *J. Phys. Condens. Matter* **2009**, *21*, 084204. [CrossRef] [PubMed]

34. Momma, K.; Izumi, F. VESTA 3 for three-dimensional visualization of crystal, volumetric and morphology data. *J. Appl. Crystallogr.* **2011**, *44*, 1272–1276. [CrossRef]

35. Xia, Y.; Pan, A.; Su, Y.-Q.; Zhao, S.; Li, Z.; Davey, A.K.; Zhao, L.; Maboudian, R.; Carraro, C. In-situ synthesized N-doped ZnO for enhanced CO_2 sensing: Experiments and DFT calculations. *Sens. Actuators B Chem.* **2022**, *357*, 131359. [CrossRef]

36. Zhou, C.; Kang, J. Electronic structures of ZnO (0001)-Zn and (000−1)-O polar surfaces. *J. Mater. Sci. Mater. Electron.* **2008**, *19*, 229–233. [CrossRef]

37. Göpel, W.; Pollmann, J.; Ivanov, I.; Reihl, B. Angle-resolved photoemission from polar and nonpolar zinc oxide surfaces. *Phys. Rev. B* **1982**, *26*, 3144. [CrossRef]

38. Mora Fonz, D. A Theoretical Study on the Surfaces of Zinc Oxide. Ph.D. Thesis, University College London, London, UK, 2016.

39. Zhang, J.; Zhang, Y.; Tse, K.; Deng, B.; Xu, H.; Zhu, J. New approaches for calculating absolute surface energies of wurtzite (0001)/(0001¯): A study of ZnO and GaN. *J. Appl. Phys.* **2016**, *119*, 205302. [CrossRef]

40. Kim, M.; Hong, Y.J.; Yoo, J.; Yi, G.C.; Park, G.S.; Kong, K.j.; Chang, H. Surface morphology and growth mechanism of catalyst-free ZnO and $Mg_x Zn_{1−x} O$ nanorods. *Phys. Status Solidi RRL* **2008**, *2*, 197–199. [CrossRef]

41. Na, S.-H.; Park, C.-H. First-principles study of the surface of wurtzite ZnO and ZnS-implications for nanostructure formation. *J. Korean Phys. Soc.* **2009**, *54*, 867–872. [CrossRef]

42. Zhuang, H.; Tkalych, A.J.; Carter, E.A. Surface energy as a descriptor of catalytic activity. *J. Phys. Chem. C* **2016**, *120*, 23698–23706. [CrossRef]

43. Johnson, R.D., III. NIST Computational Chemistry Comparison And Benchmark Database, NIST Standard Reference Database Number 101, Release 16a. Available online: http://cccbdb.nist.gov/ (accessed on 14 October 2022).

44. Jin, W.; Chen, G.; Duan, X.; Yin, Y.; Ye, H.; Wang, D.; Yu, J.; Mei, X.; Wu, Y. Adsorption behavior of formaldehyde on ZnO (101‾0) surface: A first principles study. *Appl. Surf. Sci.* **2017**, *423*, 451–456. [CrossRef]

45. Chiu, C.-Y.; Wu, H.; Yao, Z.; Zhou, F.; Zhang, H.; Ozolins, V.; Huang, Y. Facet-selective adsorption on noble metal crystals guided by electrostatic potential surfaces of aromatic molecules. *J. Am. Chem. Soc.* **2013**, *135*, 15489–15500. [CrossRef] [PubMed]

46. Haynes, W.M.; Lide, D.R.; Bruno, T.J. *CRC Handbook of Chemistry and Physics*; CRC press: Boca Raton, FL, USA, 2016.

47. Fang, C.; Orhan, E.; De Wijs, G.; Hintzen, H.; De Groot, R.; Marchand, R.; Saillard, J.-Y. The electronic structure of tantalum (oxy) nitrides TaON and Ta_3N_5. *J. Mater. Chem.* **2001**, *11*, 1248–1252. [CrossRef]

48. Richter, C. Electron and Exciton Dynamics at ZnO Surfaces. Master's Thesis, Freie Universität Berlin, Berlin, Germany, 2014.

49. Deinert, J.-C. Zinc Oxide Surfaces and Interfaces: Electronic Structure and Dynamics of Excited States. Ph.D. Thesis, Technischen Universität Berlin, Berlin, Germany, 2016.

50. Deinert, J.-C.; Hofmann, O.T.; Meyer, M.; Rinke, P.; Stähler, J. Local aspects of hydrogen-induced metallization of the ZnO (101‾0) surface. *Phys. Rev. B* **2015**, *91*, 235313. [CrossRef]

51. Hoffmann, R. *Solids and Surfaces: A Chemist's View of Bonding in Extended Structures*; John Wiley & Sons: Hoboken, NJ, USA, 2021.